Editors' Suggestion

Anomalous Statistics of Sea Ice Transport are Explained by Collisional Rules

Bryan Shaddy,[1] P. Alex Greaney,[2] and Bhargav Rallabandi[2,*]

[1]*Department of Aerospace and Mechanical Engineering, University of Southern California, Los Angeles, California 90089, USA*
[2]*Department of Mechanical Engineering, University of California, Riverside, California 92521, USA*

(Received 11 December 2025; revised 21 May 2026; accepted 22 July 2026; published 10 September 2026)

Arctic sea ice fluctuates in response to its turbulent environment, leading to dispersion behaviors that are not well understood. We resolve this gap using simulations that model sea ice as a granular medium that responds to stochastic winds. Using only directly measured local environmental and ice properties as inputs, the model quantitatively reproduces the dispersion, velocity distribution, and power spectrum of sea ice observed in the Fram Strait. These transport properties are generic consequences of collisions between floes, which rapidly dissipate the energy injected by wind while shortening the mean free paths of floes. A Boltzmann transport kinetic theory yields further quantitative insight, recovering both the simulations and observations. Our findings connect floe-scale dynamics and local environmental noise to properties of sea ice at climate-relevant scales, while also establishing broader links to stochastically driven dissipative granular systems.

DOI: 10.1103/g8y2-8ytt

The transport of sea ice plays a crucial role in ecology and global climate [1,2]. The ice cover consists of meter-thick floes that range in size from several meters to a few kilometers across. Turbulent winds—and to a lesser extent, ocean currents—drive the stochastic motion of the ice, which leads to its dispersion across the polar oceans. Velocity fluctuations of sea ice are strongly correlated with those of the wind, e.g., in the Fram Strait [3]. However, ice velocity distributions are non-Gaussian, despite the normally distributed winds. Observations reveal other puzzling features [3–6]; e.g., the diffusivity and power spectrum of ice differ significantly (sometimes by an order of magnitude) from random-walk models. These discrepancies make the prediction of ice transport challenging on climatically relevant scales, which is exacerbated by acute changes in ice and environmental conditions in recent years [7]. Although it has been suggested that these anomalies may be associated with the intermittency of winds [8], ocean eddies [9], and ice fractures [6], the underlying mechanism remains poorly understood.

Rather than appeal to a mechanism specific to the sea ice system, we demonstrate that the observed dynamics have a *generic* physical origin in dissipative interactions between floes that respond to a stochastic environment (here, the wind). As with any dense system, interactions are important in the case of sea ice due to the large fraction φ of the ocean surface that floes occupy. In this concentrated regime, the rate of interactions far exceeds that of wind fluctuations, shortening the mean free paths of floes and draining the energy injected by wind. We show—using stochastic granular simulations and Boltzmann kinetic theory—that this paradigm *quantitatively* explains observed ice statistics. The framework contains no ad hoc terms specific to the sea ice, nor does it invoke the spatial structure of the atmospheric turbulence, but instead draws on governing physics generic to dense dissipative systems. In establishing close connections between sea ice and stochastic granular dynamics, and in advancing granular kinetic theory, we argue that the underlying principles and the dynamical features that result from them apply broadly across granular systems.

We model ice floes as rigid disks that are driven to move over the ocean surface by stochastic winds and interact through collisions [Fig. 1(a)] [10–12]. Consistent with observations [13–15] and models [16], we draw floe radii a from a power-law distribution $P_s(a) \propto a^{-2}$, between 10 m and 4500 m [Fig. 1(b)]. Aside from setting an average floe size, the detailed distribution is found to be largely unimportant (Supplemental Material [17]), but we retain it here to capture a realistic ice field. The velocity $\mathbf{v}_i$ of a floe i is driven by stresses due to winds (velocity $\mathbf{u}_i$) on its top surface, and resisted by an ocean drag on its bottom surface. We neglect ocean currents and Coriolis forces, which we find to be an adequate approximation to capture observations; see [17]. In between collisions, conservation of momentum of floe i is given by [1]

$$\rho h \frac{\mathrm{d}\mathbf{v}_i}{\mathrm{d}t} = \rho_a C_a |\mathbf{u}_i| \mathbf{u}_i - \rho_w C_w |\mathbf{v}_i| \mathbf{v}_i. \quad (1)$$

The density ρ and thickness h of the ice, the densities ρ_a and ρ_w of the atmosphere and ocean, and respective drag

*Contact author: bhargav@engr.ucr.edu

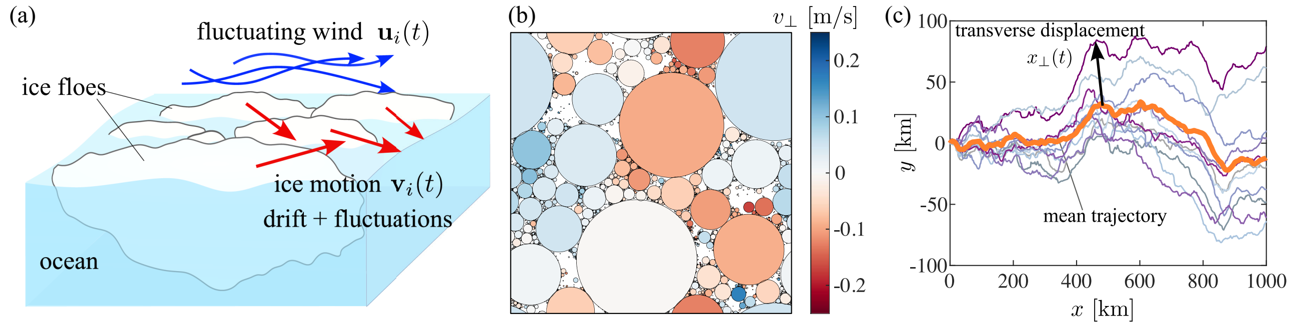

FIG. 1. (a) Fluctuating winds drive the motion of interacting ice floes on the ocean surface. (b) Snapshot of simulation showing floes (with area fraction $\varphi = 0.9$), colored by their transverse fluctuating velocities $v_\perp$. (c) Sample floe trajectories (blue-purple), indicating a mean trajectory (orange), and transverse fluctuations.

coefficients C_a and C_w are well characterized [18,19] and are tabulated in [17].

Floe-floe collisions conserve momentum but dissipate energy due to a multitude of mechanisms including deformation and fracture [20–22]. We lump these sources of dissipation in a momentum-conserving inelastic collision model [23] characterized by a dimensionless coefficient of restitution r that ranges between "perfectly inelastic" ($r = 0$) and "perfectly elastic" ($r = 1$, energy conserving) limits. When floe i (radius a_i) collides with a floe j, its postcollision velocity is

$$\mathbf{v}_i^{\text{post}} \stackrel{j}{=} \mathbf{v}_i - \frac{a_j^2}{a_i^2 + a_j^2}(1 + r)(\mathbf{v}_i - \mathbf{v}_j) \cdot \mathbf{n}\mathbf{n}, \qquad (2)$$

where $\mathbf{n}$ is the unit normal at the point of contact. We neglect melting and freezing, which are appreciable only over much longer timescales (several months) than those of interest here (days).

The turbulent winds that drive the ice motion have a complex spatial and temporal structure. We replace these complexities with a low-order stochastic model of wind consistent with observations, which we find to be sufficient to reproduce the observed transport of ice. The ERA5 wind data [24] show that wind velocity fluctuations in the Fram Strait are approximately isotropic and normally distributed with standard deviation σ along each axis, and exponentially decorrelated on a timescale τ. Long-range spatial wind correlations manifest through a mean wind $\bar{\mathbf{u}}$, which drives the steady drift of the ice. We neglect wind gradients as they are only appreciable over the width of the strait (> 100 km), greater than the scales of interest here. By contrast, short-range wind correlations occur on length scales of ∼100 m, smaller than the mean floe size [25–27]. Thus, neighboring floes experience effectively decorrelated wind fluctuations. To capture these properties, we model the wind as an Ornstein-Uhlenbeck random field (time-colored noise), governed by the Langevin equation [28–30]

$$\frac{\mathrm{d}\mathbf{u}_i}{\mathrm{d}t} = \frac{\bar{\mathbf{u}} - \mathbf{u}_i}{\tau} + \sqrt{\frac{2\sigma^2}{\tau}}\boldsymbol{\eta}_i(t), \qquad (3)$$

where $\boldsymbol{\eta}_i(t)$ is a two-dimensional (2D) standard white noise with unit variance.

In summary, the model represents sea ice as a 2D inelastic granular medium driven by a colored-noise forcing (due to wind) and resisted by drag (due to the ocean). We solve (3) to generate statistically well-controlled stochastic winds, which we then use to drive the ice dynamics (1), subject to the collision rule (2). We simulate the motion of $N = 2000$ (large enough to ensure statistical convergence) interacting ice floes at a fixed area fraction φ in a periodic domain of side $L = (\sum_i \pi a_i^2/\varphi)^{1/2}$, typically between 18 and 50 km, within the mesoscale regime where (3) applies [Fig. 1(b)]. To compare our model results with observations, we focus on the Fram Strait in January–March of the years 2002–2003 and 2007–2009, where ice transport data from the FRAMZY and ACSYS campaigns were analyzed in [3]. We analyze the ERA5 dataset [24] in the same region and time to extract a mean wind speed $\bar{u} \approx 4.8$ m/s, a standard deviation $\sigma \approx 6.0$ m/s and a correlation time $\tau \approx 32$ h (data analysis in [17]). We simulate a range of φ, noting that observed ice fractions in the Fram Strait vary about a mean of about 0.9 (cf. Fig. 7 of [3]). Thus, all model inputs are obtained from field, satellite or reanalysis data, with the sole exception of the coefficient of restitution r, which we set to 0.1.

Scaling analysis of (1) identifies the Nansen number $\mathcal{N} = \sqrt{(\rho_a C_a/\rho_w C_w)} \approx 0.02$ as the ratio of the characteristic ice drift speed to the wind speed, and an inertial relaxation timescale $\tau_d = (\rho h \mathcal{N}/\rho_a C_a \bar{u}) \approx 1.2$ h, over which floes adjust to the wind [17]. Before discussing the simulations we analyze the dilute limit ($\varphi \to 0$), where collisions are absent. Because of their short inertial relaxation time ($\tau_d \ll \tau$), floes adjust quasistatically to wind fluctuations, reducing (1) to $\mathbf{v}_i \approx \mathcal{N}\mathbf{u}_i$. Using this relation in (3) yields a stochastic differential equation for ice velocity fluctuations $\mathbf{v}_i'$,

$$\frac{\mathrm{d}\mathbf{v}_i'}{\mathrm{d}t} \approx -\frac{\mathbf{v}_i'}{\tau} + \sqrt{\frac{2\mathcal{N}^2\sigma^2}{\tau}}\boldsymbol{\eta}_i(t). \text{ (dilute limit)} \tag{4}$$

Floes fluctuate both along and across the drift direction. We focus on their transverse fluctuating velocities $v_\perp(t)$, which satisfy the one-dimensional (1D) form of (4). Equation (4) shows that in the dilute limit, ice floes follow Langevin dynamics with rms velocity $v_0^{\mathrm{rms}} = \mathcal{N}\sigma$ and diffusivity $D_0 = \mathcal{N}^2\sigma^2\tau$. These are characteristic scales of the stochastic ice motion in the dilute limit; for the parameters of the Fram Strait, they are about 12 cm/s and 1580 m^2/s, respectively. However, the observed rms velocity is about half as large as v_0^{rms}, while the observed diffusivity is more than an order of magnitude smaller than D_0. We will see that floe-floe collisions are responsible for these discrepancies, and that simulations at realistic φ quantitatively match observations.

From the simulated floe trajectories, we extract fluctuating ice displacements $x_\perp(t)$ and velocities $v_\perp(t)$ transverse to the mean [Fig. 1(c)], which we use to compute macroscopic transport properties of the ice (defined in [17]). We compare the results of this analysis with ice observations in the Fram Strait for a region and time consistent with the model inputs [3]. We also plot IABP ice data in the central Arctic [3], which show similar trends despite being geographically different (cf. Figs. 2–4). All ice data plotted here are taken directly from [3].

The transverse mean squared displacement (MSD) $\langle x_\perp^2\rangle$ (angle brackets denote an ensemble average) quantifies the dispersion of ice floes away from the mean trajectory [Fig. 1(c)]. After an initial ballistic transient (MSD $\propto t^2$), the dispersion becomes diffusive (MSD $\sim 2Dt$), characterized by a transverse diffusivity D (Fig. 2). At small φ, the simulations recover the theoretical result for isolated floes $D \approx D_0 = 1580\ \mathrm{m}^2/\mathrm{s}$. (As noted earlier, this is an order of magnitude greater than observed in the Fram Strait.) Increasing φ leads to a sharp decrease in D, as collisions shorten the mean free paths of the floes. Upon matching the area fraction to the mean of the observations ($\varphi = 0.9$), the simulations *quantitatively* reproduce the observed MSD [Fig. 2(a)]. Simulations yield diffusivities in the range 40–100 m^2/s ($0.025D_0$ to $0.063D_0$) over a range of ice concentrations $0.84 < \varphi < 0.92$ [Fig. 2(b)], consistent with observations over the same range of φ [3].

Next, we study the transverse power spectral density (PSD) as a function of the temporal frequency f (Fig. 3). Simulations are again in quantitative agreement with observations at $\varphi = 0.9$ (with the same model inputs as before, and no additional fitting) across timescales ranging from a few hours to 10 days. The PSD exhibits an f^{-1} scaling that transitions to an f^{-2} scaling at around 70 μHz. Neglecting collisions (gray curve in Fig. 3) significantly overpredicts observations at low frequencies and underpredicts them at high frequencies. Collisions flatten the spectrum by decreasing the diffusivity (the low-f limit) while boosting high-f contributions due to the shorter mean free paths of the floes. The peak in the observed PSD at $(12\ \mathrm{h})^{-1} \approx 23$ μHz is likely from tidal effects; see Ref. [17].

Finally, we analyze the distribution of transverse ice velocities (Fig. 4). At a statistical steady state, the rate of energy injected by wind $\dot{\mathcal{E}}_{\mathrm{wind}}$ is dissipated by ocean drag $\dot{\mathcal{E}}_{\mathrm{ocean}}$ and collisions $\dot{\mathcal{E}}_{\mathrm{coll}}$. For small ice fractions, collisions are infrequent, so floes adjust rapidly to wind fluctuations. This leads to a normal distribution of ice velocities $\propto e^{-qv_\perp^2}$ reflecting that of the wind, consistent with (4). As φ increases, collisions become more frequent and dissipate a greater fraction of the energy injected by wind. This leads to slower floes on average, causing the PDF to become narrower (smaller v^{rms}) as shown in Fig. 4(b). Additionally, the *shape* of the PDF changes at higher φ: it is no longer Gaussian, but instead has exponential tails ($\propto e^{-k|v_\perp|}$), mirroring observations of sea ice [3,6]. With the same parameters as before ($\varphi = 0.9$, without additional fitting), the simulations replicate the observed velocity PDF in the

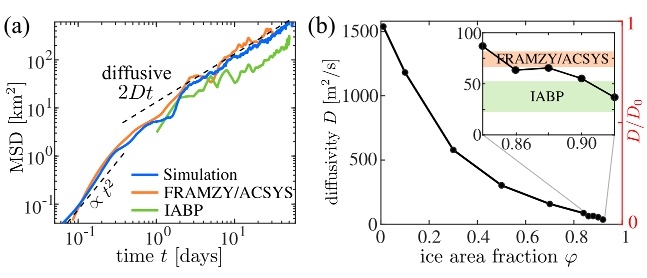

FIG. 2. Dispersion. (a) Transverse MSD, showing observations and simulations (at $\varphi = 0.9$). The MSD is diffusive ($\sim 2Dt$) after a short ballistic transient. (b) Diffusivity D decreases sharply with ice area fraction φ. The inset shows data for φ between 0.84 and 0.92, indicating simulations (symbols) and the range of observations (shaded regions).

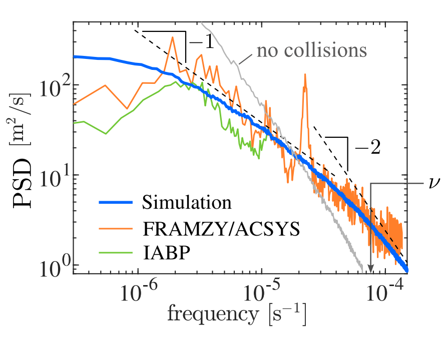

FIG. 3. Power spectral density. Simulations ($\varphi = 0.9$) capture observations in the Fram Strait [3] over 2 decades of frequency f. The transition from f^{-1} to f^{-2} scaling occurs close to the collision frequency $\nu \approx 75$ μHz. Neglecting collisions (gray curve) overpredicts the PSD at low f and underpredicts it at higher f.

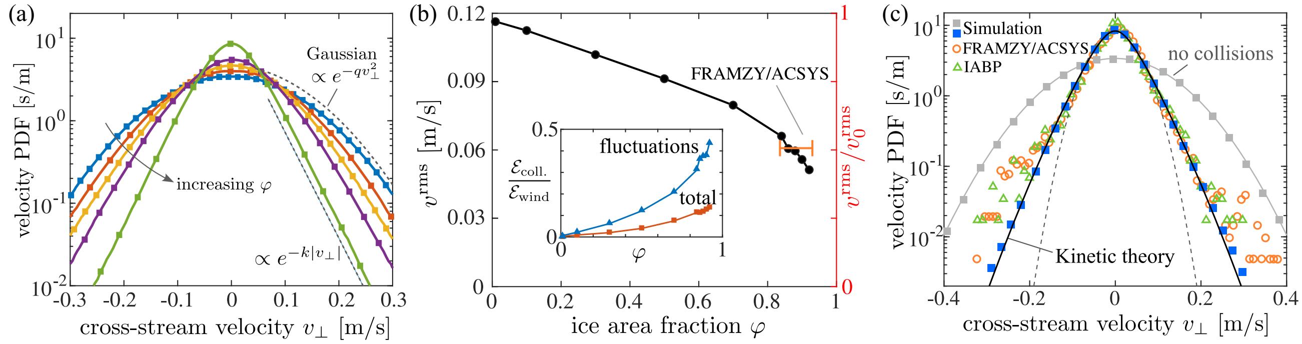

FIG. 4. Velocity distribution. (a) Transverse ice velocity PDF narrows with increasing ice fraction φ, while also transitioning between Gaussian and exponential tails. (b) The rms velocity decreases with φ and reproduces observations at $\varphi = 0.9$. A greater fraction of the work done by the wind is dissipated by collisions at larger φ (inset). (c) Velocity PDF from simulations ($\varphi = 0.9$) and kinetic theory (solid curve) match observations in the Fram Strait [3]. These distributions are simultaneously much wider than the best-fit Gaussian (dashed curve), and much narrower than the Gaussian PDF without collisions (gray symbols and curve).

Fram Strait [3] [Fig. 4(c)]. This distribution is much narrower than in the dilute limit (gray symbols and curves), while simultaneously being much wider than the best-fit Gaussian (dashed curve). The model yields an rms velocity of about $5.6-6.0$ cm/s (about half the dilute limit $v_0^{\rm rms}$), within 10% of observations [Fig. 4(b)].

To further test the model, we compare with the ice data of [9] in the marginal ice zone off the eastern coast of Greenland during April–July in the years 2003–2020. They find $v^{\rm rms}$ in the range of 4–9 cm/s for ice fractions $\varphi \in (0.1, 0.95)$; cf. Fig. 15 of [9]. From the ERA5 wind data in this region and time, we extract a wind fluctuation velocity $\sigma \approx 4.5$ m/s. Our model gives $v_0^{\rm rms} = \mathcal{N}\sigma \approx$ 9 cm/s (the dilute limit), with which we estimate, using Fig. 4(b), that $v^{\rm rms}$ is in the range 4.3–8.5 cm/s over the same range of φ, consistent with observations.

Thus, the simulations simultaneously recover the observed dispersion, power spectrum, and velocity distribution with a single free parameter r, with all other inputs taken directly from data. The coefficient of restitution r only weakly affects the results as long as it is not too close to unity (the non-dissipative limit); see [17]. As noted earlier, polydispersity of floe sizes is also not essential to the statistics of motion. A floe's momentum scales with its area, while the rate of collisional momentum exchange depends on the number of neighbors, which scales with its perimeter. An effective floe radius with the average momentum-exchange properties of the floe population is given by the area-to-perimeter ratio $\bar{a} = (\langle a^2 \rangle / \langle a \rangle) \approx$ 735 m. Simulations that replace the power-law size distribution by a single floe radius of 750 m (within 2% of $\bar{a}$) still accurately capture the observations; see [17].

These findings show that the signatures of stochastic sea ice motion are generic features of granular collisions forced by a time-colored noise (the wind) subject to drag (the ocean). In fact, similar velocity distributions have been observed in other dissipative granular systems [31–34]. We exploit this connection to develop a kinetic theory for a spatially uniform population of equally sized floes with a distribution of velocities. One way to account for interactions is to introduce a coarse-grained interaction force into (4), e.g., [35]. Rather than model such a force, we follow [36–39] and use the collision framework to formulate these interactions directly at the level of kinetic theory. We introduce a probability density $P(v_\perp, t)$ to describe the distribution of transverse velocities at time t. Applying standard techniques of stochastic calculus [28] (p. 147) to the 1D form of (4) yields a partial differential equation governing $P(v_\perp, t)$ for a system of momentum-exchanging floes,

$$\frac{\partial P}{\partial t} = \frac{\partial}{\partial v_\perp}\left(\frac{v_\perp P}{\tau}\right) + \frac{\mathcal{N}^2\sigma^2}{\tau}\frac{\partial^2 P}{\partial v_\perp^2} + Q[v_\perp]. \qquad (5)$$

This is a generalized Boltzmann transport equation (BTE), where we have introduced the *collision operator* Q to account for the redistribution of floe velocities due to collisions. Note that Q must be conservative ($\int Q \mathrm{d}v_\perp = 0$) for P to represent a probability density. We see that (5) retrieves the Fokker-Planck equation and the classical BTE [23] in the respective limits of no collisions ($Q = 0$) and no wind fluctuations ($\sigma = 0$).

We express Q as a combination of (i) a rate of loss L of floes with velocity $v_\perp$ because they collide with other floes and acquire a new velocity, and (ii) a rate of gain G from floes acquiring velocity $v_\perp$ as a result of collision. Floes in concentrated ice fields undergo many collisions within the long wind correlation time. Thus, each floe samples the entire distribution of ice velocities through collisions, so Q becomes linear in the distribution [36,38,39]; see [17] for a discussion. Floes are removed from the distribution at a rate $L = \nu P(v_\perp, t)$, where ν is a collision rate with units of inverse time. Collisions dissipate energy and thus slow down floes on average. Let α^{-1} denote the fractional reduction in speed per collision, so a floe with velocity $v_\perp$ is gained from a precollision floe of velocity $\alpha v_\perp$. Since P is a density, this contraction contributes a Jacobian factor α, giving $G = \alpha\nu P(\alpha v_\perp, t)$. Writing $Q = G - L$, (5) reduces at steady state to

$$(\mathcal{N}\sigma)^2 \frac{\mathrm{d}^2 P(v_\perp)}{\mathrm{d}v_\perp^2} + \frac{\mathrm{d}[v_\perp P(v_\perp)]}{\mathrm{d}v_\perp} + \nu\tau[\alpha P(\alpha v_\perp) - P(v_\perp)] = 0, \tag{6}$$

which is a linear but nonlocal differential equation for $P(v_\perp)$ similar to that of [34]. The first two terms account for wind noise and ocean drag. The third term is due to the collision operator Q; it is indeed conservative.

Because the velocity distribution is peaked around zero, a floe with velocity $v_\perp$ is most likely to collide with a relatively slow (effectively stationary) floe, reducing the kinetic energy of the pair by a factor $(1 + r^2)/2$. To relate α to r, we picture such a collision as distributing the incident momentum over α floes (see Supplemental Material [17]), each slowed to $v_\perp/\alpha$, so that momentum is conserved and the energy falls by α^{-1}. Equating the two energy factors gives $\alpha = 2/(1 + r^2)$. In the elastic limit $r = 1$, this estimate gives $\alpha = 1$ and the collision operator vanishes as expected. For $r = 0.1$ used in simulations, $\alpha = 1.98$. The collision rate ν is the inverse of a typical collision time, and depends on the mean free path of a floe and the speed of fluctuations. Assuming a square lattice of floes with a typical rms velocity of $\mathcal{N}\sigma$ yields a rough estimate $\nu \approx \sqrt{(\varphi/\pi)}[\mathcal{N}\sigma/\bar{a}]$. In the dilute limit, $\nu = 0$ and (6) admits a Gaussian distribution $P(v_\perp) \propto \mathrm{e}^{-v_\perp^2/(2\mathcal{N}^2\sigma^2)}$ consistent with simulations [Fig. 4(c)]. The collision term becomes important at nonzero φ. In this case we solve (6) numerically to find narrower PDFs with exponential tails. For inputs consistent with the Fram Strait, the above estimate gives $\nu \approx 85$ μHz. This is close to the best-fit value $\nu = 75$ μHz $= 0.27$ hr^{-1}, at which the kinetic theory (6) is virtually indistinguishable from the simulations and captures the observed velocity PDF [Fig. 4(c)]. Note that ν is close to the crossover frequency in the PSD (Fig. 3).

In the concentrated regime, the collision rate greatly exceeds the wind decorrelation rate, $\nu\tau \gg 1$. We obtain analytic insight in this regime using a WKB analysis [40] of (6), which shows that collisions, not ocean drag, are the primary source of energy dissipation [17]. The analysis yields an exponentially tailed velocity PDF $P(v_\perp) = \frac{1}{2}k\exp\{-k|v_\perp|\}$ with $k = \sqrt{\nu\tau - 1}/(\mathcal{N}\sigma)$, consistent with simulations. From this distribution we obtain an analytic prediction for the rms ice velocity

$$v^{\mathrm{rms}} = \sqrt{\frac{2}{\nu\tau - 1}}\mathcal{N}\sigma \approx \sqrt{\frac{2}{\sqrt{\varphi/\pi}\mathcal{N}\sigma\tau/\bar{a} - 1}}\mathcal{N}\sigma. \tag{7}$$

For the Fram Strait inputs and the best-fit ν, (7) yields $v^{\mathrm{rms}} \approx 6.0$ cm/s, in excellent agreement with observations, simulations and solutions of (6); cf. Fig. 4(b). To close the loop, we reinterpret the motion of a floe in a concentrated ice field in terms of Langevin dynamics with the new rms velocity $\sqrt{2/(\nu\tau - 1)}\mathcal{N}\sigma$ and relaxation time ν^{-1} (as opposed to the rms velocity $\mathcal{N}\sigma$ and relaxation time τ of the dilute limit). This yields a diffusivity

$$D = \frac{(v^{\mathrm{rms}})^2}{\nu} \approx \frac{2\sqrt{\pi/\varphi}\mathcal{N}\sigma\bar{a}}{(\sqrt{\varphi/\pi}\mathcal{N}\sigma\tau/\bar{a} - 1)}. \tag{8}$$

With the same inputs (8) gives $D \approx 48$ m^2/s, close to the simulated result at $\varphi = 0.9$ (55 m^2/s). The analytic predictions are independent of r, mirroring the insensitivity of simulations to this parameter [17]. In the limit of large collision rates ($\nu\tau \gg 1$) the theory yields scaling laws $v^{\mathrm{rms}}/v_0^{\mathrm{rms}} \propto (\nu\tau)^{-1/2}$ and $D/D_0 \propto (\nu\tau)^{-2}$. Thus, collisions suppress the diffusivity much more strongly than they do velocity fluctuations, consistent with simulations [Figs. 2(b) and 4(b)].

We have shown that transport properties of concentrated sea ice are generic consequences of rapid dissipative interactions between floes responding to fluctuating winds. At high concentrations, the rate of collisions greatly exceeds that of wind fluctuations. These collisions shorten mean free paths and dissipate the energy injected by wind, quantitatively reproducing observed ice dispersion, power spectra, and velocity distributions. We reiterate that the model inputs are extracted directly from observational data, with the exception of a single free parameter that only weakly influences the results. The model inputs are informed by a small number of *local* wind properties, underscoring that ice dispersion is controlled by stochastic mechanisms at the floe scale, rather than the large-scale spatial structure of the ice, ocean, or wind fields. While ocean currents and eddies may also contribute to ice translation and rotation [9,41], their influence on the data considered here appears secondary. Large-scale ocean circulations such as the Beaufort gyre may modify the predicted transport properties in a scale-dependent way [42], analogous to Taylor-Aris dispersion. A systematic study of these effects, and an interrogation of the model across different geographical regions, times, and ice conditions, are left to future work.

Our findings are useful in resolving sea ice processes below the resolution of climate models, and in predicting ice transport from coarsely resolved environmental data. Further understanding of how floe-scale interactions affect large-scale ice transport promises new physical insights into mechanisms important to global climate. More broadly, our model maps the dynamics of sea ice to those of a stochastically forced granular medium, so its findings should also apply to granular systems beyond sea ice. Our treatment of the Boltzmann collision operator identifies features that are generic to systems with frequent energy-dissipating interactions between objects in complex and noisy flow environments. Such processes are important in a several applications, such as the flow of particle-laden inks for 3D printing, avalanches and landslides, active matter systems, and transport problems in materials science and nuclear engineering. Our methods and findings may thus be useful in understanding emergent transport properties across a broad range of dissipative systems.

Acknowledgments—We thank M. M. Wilhelmus and E. Ben-Naim for preliminary discussions. B. R. thanks the UCR Regents Faculty Fellowship and the Hellman Foundation for support. B. S. thanks the UCR Chancellor's Research Fellowship, and the USC Viterbi School of Engineering Graduate Fellowship for Incoming Students.

Data availability—There are no publicly available research data or software supporting this manuscript. Requests for further information or data should be sent to the authors.

[1] J. Weiss, *Drift, Deformation, and Fracture of Sea Ice: A Perspective Across Scales* (Springer, New York, 2013), Vol. 83.
[2] N. Untersteiner, *The Geophysics of Sea Ice* (Springer, New York, 2013).
[3] A. Gabrielski, G. Badin, and L. Kaleschke, Anomalous dispersion of sea ice in the Fram Strait region, J. Geophys. Res. **120**, 1809 (2015).
[4] M. S. Swenson and P. P. Niiler, Statistical analysis of the surface circulation of the California Current, J. Geophys. Res. **101**, 22631 (1996).
[5] A. Bracco, J. LaCasce, and A. Provenzale, Velocity probability density functions for oceanic floats, J. Phys. Oceanogr. **30**, 461 (2000).
[6] P. Rampal, J. Weiss, and D. Marsan, Arctic sea ice velocity field: General circulation and turbulent-like fluctuations, J. Geophys. Res. **114**, C10014 (2009).
[7] H. Sumata, L. De Steur, D. V. Divine, M. A. Granskog, and S. Gerland, Regime shift in Arctic Ocean sea ice thickness, Nature (London) **615**, 443 (2023).
[8] A. Womack, A. Alberello, M. de Vos, A. Toffoli, R. Verrinder, and M. Vichi, A contrast in sea ice drift and deformation between Winter and Spring of 2019 in the Antarctic marginal ice zone, Cryosphere **18**, 205 (2024).
[9] D. M. Watkins, E. M. Buckley, M. Kim, J. K. Hutchings, and M. M. Wilhelmus, Characterizing the marginal ice zone in the Greenland Sea through seasonal floe-scale sea ice observations, J. Glaciol. 1 (2026).
[10] A. Herman, Molecular-dynamics simulation of clustering processes in sea-ice floes, Phys. Rev. E **84**, 056104 (2011).
[11] A. Damsgaard, A. Adcroft, and O. Sergienko, Application of discrete element methods to approximate sea ice dynamics, J. Adv. Model. Earth Syst. **10**, 2228 (2018).
[12] N. Chen, S. Fu, and G. Manucharyan, Lagrangian data assimilation and parameter estimation of an idealized sea ice discrete element model, J. Adv. Model. Earth Syst. **13**, e2021MS002513 (2021).
[13] D. Rothrock and A. Thorndike, Measuring the sea ice floe size distribution, J. Geophys. Res. **89**, 6477 (1984).
[14] T. Toyota, S. Takatsuji, and M. Nakayama, Characteristics of sea ice floe size distribution in the seasonal ice zone, Geophys. Res. Lett. **33**, L02616 (2006).
[15] M. Gherardi and M. C. Lagomarsino, Characterizing the size and shape of sea ice floes, Sci. Rep. **5**, 10226 (2015).
[16] S. Brenner, C. Horvat, P. Hall, A. Lo Piccolo, B. Fox-Kemper, S. Labbé, and V. Dansereau, Scale-dependent air-sea exchange in the polar oceans: Floe-floe and floe-flow coupling in the generation of ice-ocean boundary layer turbulence, Geophys. Res. Lett. **50**, e2023GL105703 (2023).
[17] See Supplemental Material at http://link.aps.org/supplemental/10.1103/g8y2-8ytt for dimensional analysis, wind data analysis, parameter studies, and a discussion of the kinetic theory.
[18] S. Toppaladoddi and J. S. Wettlaufer, Theory of the sea ice thickness distribution, Phys. Rev. Lett. **115**, 148501 (2015).
[19] M. Leppäranta, *The Drift of Sea Ice* (Springer Science & Business Media, New York, 2005).
[20] D. Vella and J. S. Wettlaufer, Finger rafting: A generic instability of floating elastic sheets, Phys. Rev. Lett. **98**, 088303 (2007).
[21] D. Vella and J. S. Wettlaufer, Explaining the patterns formed by ice floe interactions, J. Geophys. Res. **113**, C11011 (2008).
[22] B. Auvity, L. Duchemin, A. Eddi, and S. Perrard, Wave-induced fracture of a sea-ice analog, Phys. Rev. Lett. **136**, 014101 (2026).
[23] C. Villani, Mathematics of granular materials, J. Stat. Phys. **124**, 781 (2006).
[24] H. Hersbach, B. Bell, P. Berrisford, G. Biavati, A. Horányi, J. Muñoz Sabater, J. Nicolas, C. Peubey, R. Radu, I. Rozum, D. Schepers, A. Simmons, C. Soci, D. Dee, and J.-N. Thépaut, ERA5 hourly data on single levels from 1979 to present, Copernicus Climate Change Service (C3S) Climate Data Store (CDS) (2018) (Accessed on 12-Sep-2021).
[25] R. Flay and D. Stevenson, Integral length scales in strong winds below 20 m, J. Wind Eng. Ind. Aerodyn. **28**, 21 (1988).
[26] L. M. Bardal and L. R. Sætran, Spatial correlation of atmospheric wind at scales relevant for large scale wind turbines, J. Phys. Conf. Ser. **753**, 032033 (2016).
[27] R. Thedin, E. Quon, M. Churchfield, and P. Veers, Investigations of correlation and coherence in turbulence from a large-Eddy simulation, Wind Energy Sci. **8**, 487 (2023).
[28] M. D. Graham, *Microhydrodynamics, Brownian Motion, and Complex Fluids* (Cambridge University Press, Cambridge, England, 2018), Vol. 58.
[29] R. Zárate-Miñano and F. Milano, Construction of SDE-based wind speed models with exponentially decaying autocorrelation, Renewable Energy **94**, 186 (2016).
[30] R. Calif, PDF models and synthetic model for the wind speed fluctuations based on the resolution of Langevin equation, Applied Energy **99**, 173 (2012).
[31] K. Ichiki and H. Hayakawa, Dynamical simulation of fluidized beds: Hydrodynamically interacting granular particles, Phys. Rev. E **52**, 658 (1995).

[32] J. S. Van Zon and F. C. MacKintosh, Velocity distributions in dissipative granular gases, Phys. Rev. Lett. **93**, 038001 (2004).

[33] A. Kawarada and H. Hayakawa, Non-gaussian velocity distribution function in a vibrating granular bed, J. Phys. Soc. Jpn. **73**, 2037 (2004).

[34] K. Kohlstedt, A. Snezhko, M. V. Sapozhnikov, I. S. Aranson, J. S. Olafsen, and E. Ben-Naim, Velocity distributions of granular gases with drag and with long-range interactions, Phys. Rev. Lett. **95**, 068001 (2005).

[35] S. Toppaladoddi, A viscous continuum theory of sea ice motion based on stochastic floe dynamics, J. Fluid Mech. **1014**, A6 (2025).

[36] T. Van Noije and M. Ernst, Velocity distributions in homogeneous granular fluids: The free and the heated case, Granular Matter **1**, 57 (1998).

[37] N. V. Brilliantov and T. Pöschel, *Kinetic Theory of Granular Gases* (Oxford University Press, New York, 2004).

[38] E. Ben-Naim, B. Machta, and J. Machta, Power-law velocity distributions in granular gases, Phys. Rev. E **72**, 021302 (2005).

[39] E. Ben-Naim and J. Machta, Stationary states and energy cascades in inelastic gases, Phys. Rev. Lett. **94**, 138001 (2005).

[40] C. M. Bender and S. A. Orszag, *Advanced Mathematical Methods for Scientists and Engineers I: Asymptotic Methods and Perturbation Theory* (Springer Science & Business Media, New York, 1999).

[41] G. E. Manucharyan, R. Lopez-Acosta, and M. M. Wilhelmus, Spinning ice floes reveal intensification of mesoscale eddies in the western Arctic Ocean, Sci. Rep. **12**, 7070 (2022).

[42] S. Martin and A. S. Thorndike, Dispersion of sea ice in the Bering Sea, J. Geophys. Res. **90**, 7223 (1985).

Supplemental Material: Anomalous statistics of sea ice transport are explained by collisional rules

Bryan Shaddy,[1] P. Alex Greaney,[2] and Bhargav Rallabandi[2,*]

[1]*Department of Aerospace and Mechanical Engineering, University of Southern California, Los Angeles, California 90089, USA*

[2]*Department of Mechanical Engineering, University of California, Riverside, California 92521, USA*

I. INTRODUCTION

Here we include a scaling analysis of the ice dynamics (Sec. II), details of the numerical methods used in the simulations (Sec. III), formal definitions of transport properties (Sec. IV), model inputs and details of the analysis used to extract wind data (Sec. V), investigation of the roles of the area fraction, coefficient of restitution, floe size distribution, and Coriolis forces (Sec. VI), and an extended discussion and analysis of the kinetic theory (Sec. VII).

II. SCALING ANALYSIS OF THE ICE DYNAMICS

Accounting for ocean current, Coriolis forces, and ocean tilt, the governing equation for the motion of a single floe (valid in between collisions) is given by

$$\rho h \frac{\mathrm{d}\mathbf{v}}{\mathrm{d}t} = \rho_a C_a(\mathbf{u}-\mathbf{v})|\mathbf{u}-\mathbf{v}| - \rho_w C_w(\mathbf{v}-\mathbf{w})|\mathbf{v}-\mathbf{w}| - \rho h f_C\, \mathbf{k}\times\mathbf{v} - \rho g h \mathbf{s}. \tag{S1}$$

Here, $\mathbf{w}$ is the velocity of the water, $f_C = 2\Omega\sin\phi$ is the Coriolis frequency at the latitude ϕ due to the rotation of the Earth with angular velocity Ω and $\mathbf{k}$ is the unit vector normal to the ocean surface. Also, $\mathbf{s}$ is the ocean surface gradient, which produces a force on the floe due to gravity. We observe that the wind and ocean drag forces now depend on the relative velocity between ice and the air or water, respectively. Note that we have neglected turning angles in the drag forces for simplicity, but these effects are secondary and do not affect the scaling analysis below.

To understand the relative importance of the various terms we non-dimensionalize (S1). We use the mean wind and ocean speeds, $\overline{u}$ and $\overline{w}$, to scale $\mathbf{u}$ and $\mathbf{w}$. The typical ice speed is $\mathcal{N}\overline{u}$, where $\mathcal{N}$ is the Nansen number (defined in the main text and in the equation below). We scale time by the ice dynamic timescale $\tau_d = \rho h/(\overline{u}\sqrt{\rho_a\rho_w C_a C_w})$, which represents the time needed for a floe to adjust to a change in wind speed. Also, we denote the typical sea surface gradient by s^*. Using uppercase symbols for dimensionless variables, the rescaled form of (S1) is

$$\frac{\mathrm{d}\mathbf{V}}{\mathrm{d}T} = (\mathbf{U}-\mathcal{N}\mathbf{V})\,|\mathbf{U}-\mathcal{N}\mathbf{V}| - (\mathbf{V}-\beta\mathbf{W})\,|\mathbf{V}-\beta\mathbf{W}| - \mathcal{K}\mathbf{k}\times\mathbf{V} - \mathcal{G}\mathbf{S}, \quad \text{where} \tag{S2a}$$

$$\mathcal{N} \equiv \left(\frac{\rho_a C_a}{\rho_w C_w}\right)^{1/2}, \quad \beta \equiv \frac{\overline{w}}{\mathcal{N}\overline{u}}, \quad \mathcal{K} = f_C\tau_d, \quad \text{and} \quad \mathcal{G} = \frac{g\tau_d s^*}{\mathcal{N}\overline{u}}. \tag{S2b}$$

The Nansen number $\mathcal{N}$ is the ratio of the characteristic ice drift speed to the wind speed, and is about 0.02 for typical conditions in the Arctic [1]. Winds are typically on the order of 5 m/s, so the ice speed is typically about 10 cm/s.

The parameter β is the ratio of ocean current speed to ice speed. Ocean currents are often in the range of 1–10 cm/s, so β is typically smaller than unity and often smaller than about 0.5. In the present work, empirical data show that the ice fluctuations are correlated with wind fluctuations, suggesting that the influence of ocean currents is subdominant.

The dimensionless Coriolis parameter $\mathcal{K}$ is about 0.6 for typical parameters. As the Coriolis force affects all floes equally we do not expect it to contribute significantly to transport properties associated with stochasticity. We verify this in Sec. VI C below.

The typical sea surface slope is 10^{-7}–10^{-6}, so the ocean tilt parameter $\mathcal{G}$ is typically less than 0.5 and often smaller than 0.1 [1]. Additionally, ocean tilt due to tidal effects is typically on the scale of hundreds of kilometers, which is

* bhargav@engr.ucr.edu

much larger than the length scales of interest here (tens of km). Thus, over the length scales of interest here, tides appear as a spatially uniform, time-periodic (on a 12-hour period) forcing of $O(\mathcal{G})$ in the ice dynamics. Because they are spatially uniform, they do not lead to collisions and thus do not affect the dispersion and velocity distribution of ice. However, they do force the ice dynamical system at a 12-hour period, which we expect to be reflected in the peak in the PSD at this frequency (Fig. 3 of the main text).

The dominant physics are therefore captured by a balance of the wind drag and ocean drag, along with interactions between floes. Formally, taking the limits of small $\mathcal{N}$, β, $\mathcal{G}$ and $\mathcal{K}$ recovers (1) of the main text.

III. NUMERICAL IMPLEMENTATION

We initialize the ice field by placing floes (radii picked from the size distribution described in the main text) at a random selection of points in a square domain of side L. We then iteratively displace overlapping pairs of floes by a small amount normal to their line-of-centers, to obtain a non-overlapping field of floes with the desired size distribution and area fraction. Without loss of generality we orient the x axis along the constant mean wind $\bar{\mathbf{u}}$. We initialize the wind field over each ice floe as a superposition of $\bar{\mathbf{u}}$ and an isotropic pseudo-random noise with standard deviation σ. The velocity of each floe is initialized to zero.

Given the wind acting on floe i at time level (n), $\mathbf{u}_i^{(n)}$, we integrate (3) through a time step Δt according to

$$\mathbf{u}_i^{(n+1)} = \bar{\mathbf{u}} - (\bar{\mathbf{u}} - \mathbf{u}_i^{(n)})e^{-\frac{\Delta t}{\tau}} + \sigma(1 - e^{-\frac{2\Delta t}{\tau}})^{\frac{1}{2}}\mathbf{N}[0,1]. \tag{S3}$$

Here, $\mathbf{N}[0,1]$ is a standard normal random variable (zero mean, unit variance) in two dimensions. We then integrate the ice dynamics (1) through the time step Δt using a "semi-implicit" Euler integration to obtain floe velocities at time level $(n+1)$, $\mathbf{v}_i^{(n+1)}$. We then use the velocities at time levels (n) and $(n+1)$ to obtain floe positions at time level $(n+1)$. Overlapping floes at this stage are identified as having collided. To these, we apply the granular collision model (2) to obtain updated postcollision positions and velocities, thus accounting for both winds and collisions over a time-step.

We first perform a spin-up from stationary floes to arrive at a statistical equilibrium. We then reset time to zero and use velocities and positions from the statistically equilibrated state to begin a new simulation, the results of which we analyze. Our floe simulations are performed in a periodic box of side length L, so positions are tracked modulo this length. To accurately compute the MSD (which may become greater than L), we also track the number of turns each floe makes around the box along each coordinate axis. This lets us reconstruct the absolute displacement of each floe, which we use for dispersion statistics.

IV. FORMAL DEFINITIONS OF TRANSPORT PROPERTIES

The transverse mean squared displacement is the variance of the transverse displacements of the floes:

$$\mathrm{MSD}(t) = \langle x_\perp^2 \rangle = \frac{1}{N}\sum_{i=1}^{N}\left(x_{\perp,i}(t)\right)^2. \tag{S4}$$

To compute the power spectral density, we start with a time series of $v_{\perp,i}(t)$ and shift the time vector of the data by $T/2$ (T is the maximum simulated time), so that it is centered at 0. The Fourier transform of $v_{\perp,i}(t)$ over time T is

$$\hat{v}_{\perp,i}(f;T) = \int_{-T/2}^{T/2} v_{\perp,i}(t)e^{-i2\pi f t}\mathrm{d}t. \tag{S5}$$

Using the transformed velocity, we compute the power spectral density (PSD) according to

$$\mathrm{PSD}(f) = \lim_{T\to\infty}\frac{1}{T}\left\langle |\hat{v}_\perp(f;T)|^2\right\rangle. \tag{S6}$$

Note that $\int_{-\infty}^{\infty}\mathrm{PSD}(f)\mathrm{d}f = \left\langle v_\perp^2 \right\rangle$ by definition. We utilize this fact to rescale the PSD of [2] for comparison with the present results (a different normalization was used in that article).

At statistical steady state, the kinetic energy of the collection of floes remains constant with time. Thus, the rate of work done on the floes by the wind ($\dot{\mathcal{E}}_{\mathrm{wind}}$) must be equal to the rate of energy dissipated by the ocean drag ($\dot{\mathcal{E}}_{\mathrm{ocean}}$)

plus the rate of energy lost to collisions ($\dot{\mathcal{E}}_{\text{coll.}}$). Taking a dot product of wind and ocean forces on a floe i with its velocity, and adding contributions from all floes gives

$$\dot{\mathcal{E}}_{\text{wind}} = \sum_i \pi a_i^2 \rho_a C_a |\mathbf{u}_i| \mathbf{u}_i \cdot \mathbf{v}_i, \tag{S7a}$$

$$\dot{\mathcal{E}}_{\text{ocean}} = \sum_i \pi a_i^2 \rho_w C_w |\mathbf{v}_i| \mathbf{v}_i \cdot \mathbf{v}_i, \tag{S7b}$$

$$\dot{\mathcal{E}}_{\text{coll.}} = \dot{\mathcal{E}}_{\text{wind}} - \dot{\mathcal{E}}_{\text{ocean}}. \tag{S7c}$$

The (rates of) energy associated with the average motion of the floes (uniform drift) and the mean wind are obtained by replacing the wind and ice velocities by their ensemble averages. Subtracting the energy due to mean flow from the total, we obtain the energy associated with fluctuations.

V. MODEL INPUTS

A. Ice dynamic parameters

Parameters characterizing the physical sea ice system for the simulation results presented are listed in Table I [1, 3]. The ice thickness was obtained by computing the mean of the thickness distribution in [4].

Parameter	Symbol	Value
Ice density	ρ	910 kg/m^3
Ice thickness	h	2.2 m
Air density	ρ_a	1.3 kg/m^3
Air drag coefficient	C_a	1.5×10^{-3}
Water density	ρ_w	1025 kg/m^3
Water drag coefficient	C_w	5×10^{-3}

TABLE I. Input parameters to the model.

B. ERA5 Wind Data Analysis

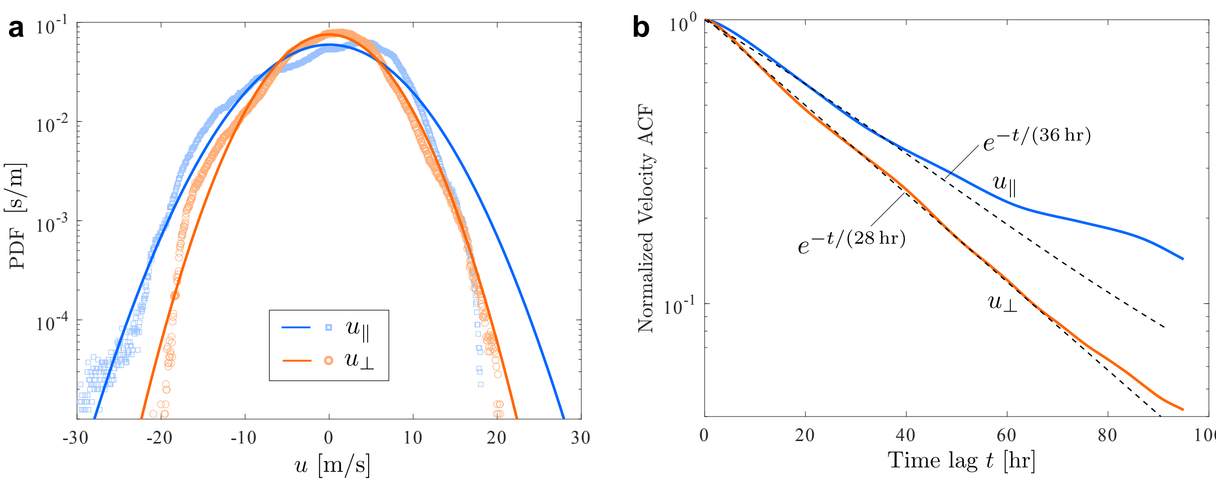

FIG. S1. (a) ERA5 $u_\parallel$ and $u_\perp$ wind velocity fluctuation PDFs (circle markers) with Gaussian fits (curves) overlaid and (b) ERA5 $u_\parallel$ and $u_\perp$ wind velocity fluctuation ACFs, plotted after normalizing by their values at $t = 0$.

The environmental inputs to the model are informed by wind statistics in the Fram Strait region (latitudes: 77° to 81°; longitudes: −5° to +5°) for the winter months of January, February, and March for the years 2002, 2003, 2007, 2008, and 2009, matching the time periods considered for the analysis of FRAMZY and ACSYS ice buoy data presented in [2]. The 10 m wind components (u_x, u_y), running in the E-W and N-S directions respectively, were analyzed from reanalysis data acquired from the ERA5 dataset [5]. We calculate the mean wind as a temporal and spatial average of the data (the mean wind speed is found to be 4.8 m/s). We then project the area-averaged time series wind vectors along and perpendicular to the mean wind (the area averaging is appropriate under practically relevant conditions, as discussed in the main text). Subtracting out the mean yields time series of streamwise $u_\parallel(t)$ and transverse $u_\perp(t)$ fluctuation velocities. We use the time series data to calculate the standard deviation and autocorrelation function (ACF, defined for a stochastic time series $u(t)$ by $\mathrm{ACF}(t) = \int u(s)u(s+t)\mathrm{d}s$.) along both directions. Figure S1 depicts the probability density function (PDF) for the wind velocity fluctuations for $u_\parallel$ and $u_\perp$. The ACF shows approximately exponential decay, which we use to determine a correlation time.

Streamwise and transverse velocity standard deviations and correlation times are approximately equal; we use an average to obtain $\sigma \approx 6.0$ m/s and $\tau \approx 32$ hr, which are used as inputs to the model.

VI. PARAMETER STUDY IN THE STOCHASTIC GRANULAR SIMULATIONS

A. Effect of area fraction and coefficient of restitution

Several aspects of the role of ice area fraction φ are studied in the main text. For these same simulations, we compute diffusivity in two different ways, (i) from a fit to the long-time dispersion $\langle x_\perp^2 \rangle \sim 2Dt$ as in the main text, and (ii) from the power spectral density at zero frequency (the Green–Kubo relation): $D = \frac{1}{2}\mathrm{PSD}(f = 0)$. Both methods yield very similar results as shown in Fig. S2(a).

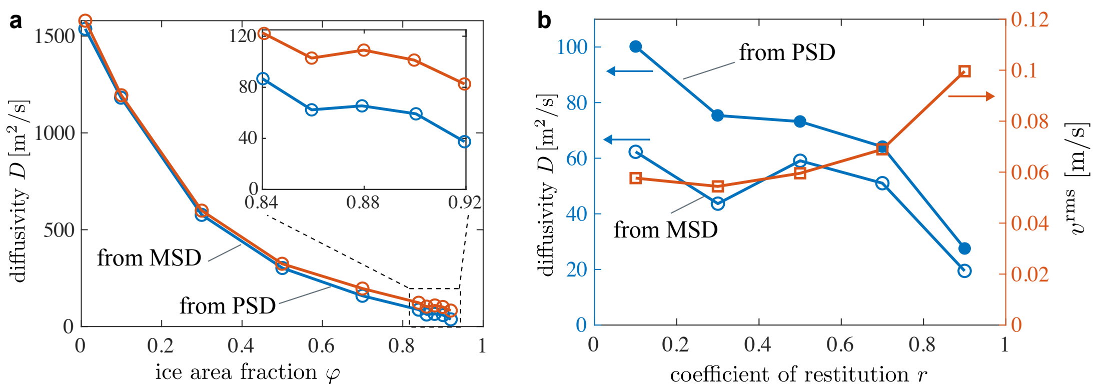

FIG. S2. Dispersion coefficient values (computed from both mean squared displacement (MSD) and power spectral density (PSD)) for polydisperse ice floes with varying input parameters. (a) D versus φ for a fixed $r = 0.1$. The inset shows the same data in the range $\varphi \in [0.84, 0.92]$, characteristic of the observational data analyzed in [2]. (b) D (left axis) and v^{rms} (right axis) versus r for a fixed $\varphi = 0.9$.

The coefficient of restitution r can range in $[0, 1]$ with 1 representing an elastic collision (no energy dissipation). Here, we consider r in $[0.1, 0.9]$ and perform simulations with all other parameters identical to the main text. When varying r at fixed $\varphi = 0.9$, we find that the dispersion coefficient does not vary significantly for r values below 0.7; see Fig. S2(b). Above this value, we find that the dispersion coefficient diminishes slightly, possibly due to the shorter mean free times. The RMS velocity is also insensitive to r for small values of r but increases somewhat as r approaches 1. It is interesting to note that the RMS velocity appears to approach about 0.12 m/s if the data is extrapolated to $r = 1$. This is about the RMS velocity of an isolated floe, as expected, since the energy of fluctuations is unaffected by collisions at $r = 1$. The same prediction is made by the kinetic theory, since the collision operator vanishes in this limit ($\alpha = 2/(1 + r^2) = 1$).

B. Simulations with a monodisperse ice floe size distribution

To examine the impact of the ice floe size distribution on dispersion statistics, simulations are repeated with uniformly sized ice floes with a single "effective" radius of 750 m. We note that this radius is close to the area-to-perimeter preserving effective radius of the full distribution, calculated to be 735 m. The maximum possible packing fraction of uniformly sized disks is ≈ 0.91 (whereas for a power law distribution the maximum possible

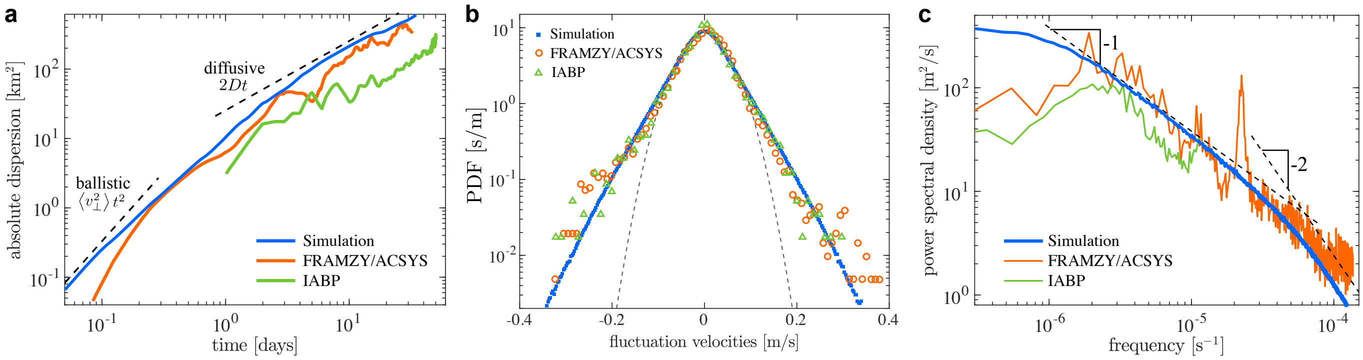

FIG. S3. Transport statistics for uniformly sized ice floes with a radius of 750 m and area fraction of 0.64. (a) Cross-stream MSD. (b) PDF for transverse velocity fluctuations (dashed curve indicates a Gaussian fit). (c) PSD for transverse velocity fluctuations.

packing fraction is close to 1). The equivalent φ for a monodisperse population is thus a free parameter. We choose $\varphi = 0.64$ in the monodisperse simulations from a fit of the monodisperse model results to the observations, all other input parameters having been carried over from the polydisperse simulations of the main text. Figure S3 depicts the resulting transverse MSD, along with the PDF and PSD for the transverse velocity fluctuations. The monodisperse results (with the adjusted φ) are clearly in good agreement with observational data [2], demonstrating the relatively small importance of the floe size distribution.

C. Effect of Coriolis forces

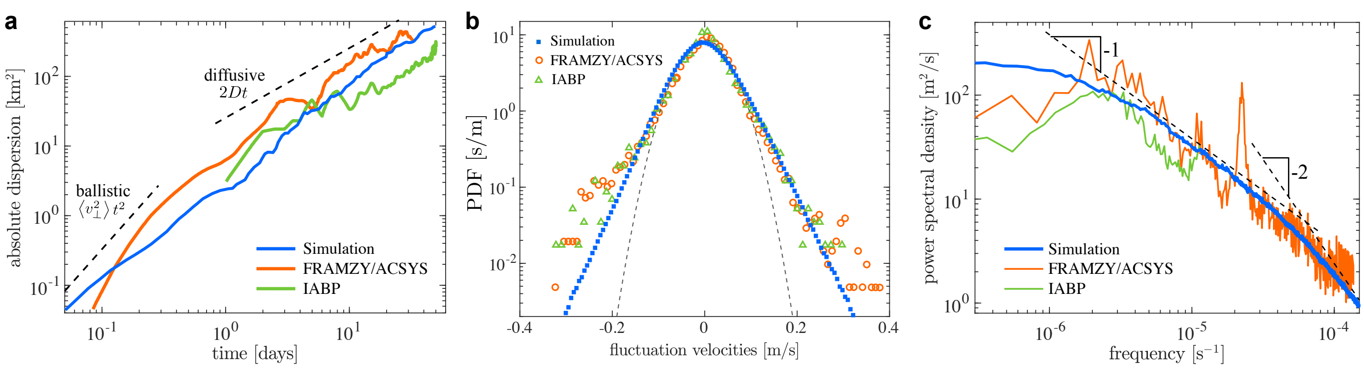

FIG. S4. Transport statistics for polydisperse floes with the inclusion of Coriolis forces. (a) Cross-stream MSD. (b) PDF for transverse velocity fluctuations (dashed curve indicates a Gaussian fit). (c) PSD for transverse velocity fluctuations.

To examine the importance of Coriolis forces, we add the Coriolis term, as described in (S2), in the reduced ice-dynamics equation (1). With the same parameters as used in the main text to compare with the Fram Strait observations ($\varphi = 0.9$, $r = 0.1$), simulations yield the dispersion statistics shown in Fig. S4. We see little difference from the results in the main text, and thus conclude that Coriolis effects are weak.

VII. DERIVATION AND ANALYSIS OF KINETIC THEORY

A. Collision operator

We start with the general two-dimensional setting. The collision operator consists of two rates: (i) a rate of loss L of floes with velocity $\mathbf{v}$ because they collide with other floes and are assigned a new velocity, and (ii) a rate of gain G from floes acquiring velocity $\mathbf{v}$ as a result of collision. The loss term is an integral over the velocity distribution weighted by the collision rate, $R(\mathbf{v} - \mathbf{v}')$, for floes with approach velocity $\mathbf{v} - \mathbf{v}'$, and the gain term is a double integral so that [6]

$$
\begin{aligned}
Q &= -L + G, \\
L &= P(\mathbf{v}) \int R(\mathbf{v} - \mathbf{v}') P(\mathbf{v}') \, \mathrm{d}\mathbf{v}', \\
G &= \int \Gamma_{\mathbf{v}', \mathbf{v}'' \to \mathbf{v}} R(\mathbf{v}' - \mathbf{v}'') P(\mathbf{v}') P(\mathbf{v}'') \, \mathrm{d}\mathbf{v}' \mathrm{d}\mathbf{v}'',
\end{aligned}
$$

where $\Gamma_{\mathbf{v}', \mathbf{v}'' \to \mathbf{v}}$ is the probability that floes colliding with velocity $\mathbf{v}'$ and $\mathbf{v}''$ result in one of those floes having postcollision velocity $\mathbf{v}$.

Collisions alter a floe's speed and direction. We posit that the angular distribution of velocities (relative to the drift velocity) must be isotropic. Collisions preserve this isotropy, so we specialize the discussion to a single component $v_\perp$ (we reuse symbols P, Q, L and G in this one-dimensional setting).

Using the full collision operator makes the BTE a nonlinear integro-differential equation that is difficult to solve, even in one dimension, so instead we replace it with a mean field approximation. We adapt the argument of [7, 8], who show that floes of velocity $v_\perp$ can be thought of — in the mean-field sense — as interacting with an effectively stationary bath of other floes. The approximation causes the loss and gain terms to become linear in the distribution, and is valid on time scales much longer than the collision time. In this setting the integral in the loss term L can be replaced with an effective total collision rate, ν, so that $L = \nu P(v_\perp)$. Collisions also dissipate energy, and so while in any individual collision a floe may get faster, when averaged over all collisions at all speeds, floes slow down. We denote the factor by which collisions slow down floes, upon an average interaction with the bath, by α^{-1}, where $\alpha > 1$. Floes with postcollision velocities in $[v_\perp, v_\perp + \mathrm{d}v_\perp]$ are thus gained from a range of precollision velocities $[\alpha v_\perp, \alpha(v_\perp + \mathrm{d}v_\perp)]$, so with a collision rate ν as before we obtain the gain rate $G = \nu\alpha P(\alpha v_\perp)$. Putting these approximations together gives the simplified form of the collision operator:

$$
Q[v_\perp] = -\nu P(v_\perp) + \nu\alpha P(\alpha v_\perp). \tag{S8}
$$

At steady state, (5) with (S8) reduces to (6). We observe that $\int Q \mathrm{d}v_\perp = 0$, which is a necessary condition for a steady-state PDF to exist.

B. Estimation of α

To relate α to the coefficient of restitution r we match energy dissipation across a collision. As the distribution is peaked around zero, a fast floe is much more likely to collide with a much slower (effectively stationary) floe, rather than with another fast floe. In one dimension it follows from (2) of the main text that a floe of velocity $v_\perp$ striking an equal-sized stationary floe produces two postcollision floes with velocities $c_- v_\perp$ and $c_+ v_\perp$, where $c_\pm = (1 \pm r)/2$. Momentum is conserved, and the kinetic energy of the pair is reduced by the factor

$$
c_+^2 + c_-^2 = \frac{1 + r^2}{2}. \tag{S9}
$$

To set the scale of α, we compare (S9) with a picture in which the collision distributes the incident momentum over α floes, each a factor α^{-1} slower than the incident floe. This picture conserves momentum, and lowers the energy by a factor $\alpha \cdot \alpha^{-2} = \alpha^{-1}$. Equating the energies yields the estimate

$$
\alpha = \frac{2}{1 + r^2}, \tag{S10}
$$

which is consistent with both the perfectly elastic ($r = 1$) and perfectly inelastic ($r = 0$) limits. At $r = 1$ we obtain $\alpha = 1$: a collision generates one floe moving at the same velocity as the incident (the other is stationary). For this α we find $Q = 0$ from (S8), which is expected since precollision and postcollision states are identical. At $r = 0$ we predict $\alpha = 2$, and indeed $c_\pm = 1/2$ there: a typical collision generates two floes, each with half the velocity of the incident floe. For the value $r = 0.1$ used in the simulations, (S10) gives $\alpha = 1.98$.

We emphasize that the momentum-conserving picture above serves only to estimate α in terms of r, and is not a derivation from (6); the operator (S8) itself conserves the number of floes, as it must for P to remain a probability density. Both ν and α are best regarded as phenomenological parameters of the mean-field closure, which may in principle also depend on the area fraction, the floe size distribution, and the dynamical timescales of the problem.

C. WKB analysis for large collision rates

We focus on the tails of the distributions, where $v_\perp$ is large relative to the RMS velocity. Since $P(v_\perp)$ decays exponentially or faster and $\alpha > 1$, $\alpha P(\alpha v_\perp)$ is exponentially smaller than $P(v_\perp)$, and thus drops out of the BTE to first approximation; see, e.g., [9]. We solve the resulting equation using a WKB procedure [10], seeking a solution of the form $P(v_\perp) = Z \exp\{f(v_\perp)\}$, where Z is a normalization factor that ensures that $\int_{-\infty}^{\infty} P(v_\perp)\mathrm{d}v_\perp = 1$. Substituting this ansatz into the simplified BTE gives

$$\mathcal{N}^2\sigma^2(f''(v_\perp) + f'(v_\perp)^2) + v_\perp f'(v_\perp) + 1 - \nu\tau = 0, \tag{S11}$$

where the prime denotes a derivative with respect to the argument. We then rescale $v_\perp = \mathcal{N}\sigma V$ and $f(v_\perp) = \gamma F(V)$, where V, F are $O(1)$ dimensionless variables, and γ is a dimensionless scaling factor that needs to be picked. Substituting yields

$$\gamma F''(V) + \gamma^2 F'(V)^2 + \gamma V F'(V) = (\nu\tau - 1). \tag{S12}$$

For rapid collisions ($\nu\tau \gg 1$), a dominant balance is struck between the second term on the left-hand side (wind fluctuations) and the term on the right (collisions). This balance yields $\gamma = \sqrt{\nu\tau - 1} \gg 1$; observe that the ocean drag term $\gamma V F'(V)$ is subdominant by $O(\gamma^{-1})$. The dominant balance identifies $F'(V)^2 \approx 1$, leading to the solution $F(V) = -|V|$. Reverting to dimensional variables gives $P(v_\perp) \sim (k/2)e^{-k|v_\perp|}, \quad \text{with} \quad k = \frac{\sqrt{\nu\tau-1}}{\mathcal{N}\sigma}$.

[1] M. Leppäranta, *The Drift of Sea Ice* (Springer Science & Business Media, 2005).

[2] A. Gabrielski, G. Badin, and L. Kaleschke, Anomalous dispersion of sea ice in the fram strait region, J. Geophys. Res.: Oceans **120**, 1809 (2015).

[3] J. Weiss, *Drift, Deformation, and Fracture of Sea Ice: A Perspective Across Scales*, Vol. 83 (Springer, 2013).

[4] S. Toppaladoddi and J. S. Wettlaufer, Theory of the sea ice thickness distribution, Phys. Rev. Lett. **115**, 148501 (2015).

[5] H. Hersbach, B. Bell, P. Berrisford, G. Biavati, A. Horányi, J. Muñoz Sabater, J. Nicolas, C. Peubey, R. Radu, I. Rozum, D. Schepers, A. Simmons, C. Soci, D. Dee, and J.-N. Thépaut, ERA5 hourly data on single levels from 1979 to present, Copernicus Climate Change Service (C3S) Climate Data Store (CDS) (2018), (Accessed on 12-Sep-2021).

[6] N. V. Brilliantov and T. Pöschel, *Kinetic Theory of Granular Gases* (Oxford University Press, 2004).

[7] T. Van Noije and M. Ernst, Velocity distributions in homogeneous granular fluids: the free and the heated case, Granul. Matter **1**, 57 (1998).

[8] E. Ben-Naim, B. Machta, and J. Machta, Power-law velocity distributions in granular gases, Phys. Rev. E **72**, 021302 (2005).

[9] K. Kohlstedt, A. Snezhko, M. Sapozhnikov, I. Aranson, J. Olafsen, and E. Ben-Naim, Velocity distributions of granular gases with drag and with long-range interactions, Phys. Rev. Lett. **95**, 068001 (2005).

[10] C. M. Bender and S. A. Orszag, *Advanced Mathematical Methods for Scientists and Engineers I: Asymptotic Methods and Perturbation Theory* (Springer Science & Business Media, 1999).